UNITED NATIONS EDUCATIONAL, SCIENTIFIC AND CULTURAL ORGANIZATION
INTERNATIONAL ATOMIC ENERGY AGENCY
INTERNATIONAL CENTRE FOR THEORETICAL PHYSICS

SMR/917 - 17

SECOND WORKSHOP ON
SCIENCE AND TECHNOLOGY OF THIN FILMS

(11 - 29 March 1996)

" XRD line broadening and texture of thin films."

presented by:

P. SCARDI
Università di Trento
Dipartimento di Ingegneria dei Materiali
38050 Mesiano (TN)
Italy

These are preliminary lecture notes, intended only for distribution to participants.

XRD LINE BROADENING AND TEXTURE OF THIN FILMS

Paolo Scardi
Dipartimento di Ingegneria dei Materiali, Università di Trento
38050 Mesiano (TN), Italy.

Abstract

Thin film microstructure deeply influences many thermo-mechanical and transport properties of technological relevance. Therefore, to optimise deposition processes and to improve the design of thin film devices, the microstructural characterisation is of paramount importance. XRD techniques offer several possibilities of non-disruptive characterisation which can be easily carried out also on a routine basis. Line broadening analysis is a useful tool to study lattice disorder, through the measurement of coherently diffracting domain (crystallite) size and microstrain, whereas texture analysis by pole figures is ideally suited to check the degree of epitaxy and growth mechanisms of thin films. In the present paper, two different cases of study will be treated: (a) epitaxial buffer layers and high T_c superconducting thin films on single crystal substrates, and (b) low texture stabilised zirconia thin films deposited at room temperature on Si wafers. The application of XRD techniques to thin film study is briefly reviewed, referring to results obtained by traditional XRD instruments employing Bragg-Brentano and parallel beam geometry.

1. Introduction

The development of thin film devices rests heavily on our ability to grow materials with the desired microstructure. In fact, the majority of thermo-mechanical and transport properties of technological concern is directly connected to features usually referred to material microstructure, namely morphology and orientation of crystalline grains and density of compositional and structural defects.

One of the most appropriate example is the close relationship between grain orientation and electrical transport properties in high T_c (HTc) superconducting materials. As shown in Figure 1, both the critical current density (J_c) at 77 K [1] and the surface resistance (R_s) at 10 GHz and 4.2 K [2], are strongly dependent on $YBa_2Cu_3O_{7-\delta}$ (YBCO) thin films grain orientation. YBCO has an orthorhombic structure, with a=3.8856 Å, b=3.8185 Å and c=11.6804 Å; as all the films were mainly made of grains with c-axis perpendicular to the

surface (c⊥), the difference among them was the in-plane orientation, expressed through $R_{100/110}$. The latter is the ratio between fractions of grains with ϕ=0° and ϕ=45° in-plane orientation; with reference to Figure 2, considering a (100) MgO (periclase) single crystal substrate, c⊥ corresponds to [001] MgO ‖ [001] YBCO, whereas the in-plane ϕ orientation is defined as [100] MgO ‖ [100] YBCO (or [010] YBCO) for ϕ=0° and [110] MgO ‖ [100] YBCO (or [010] YBCO) for ϕ=45°.

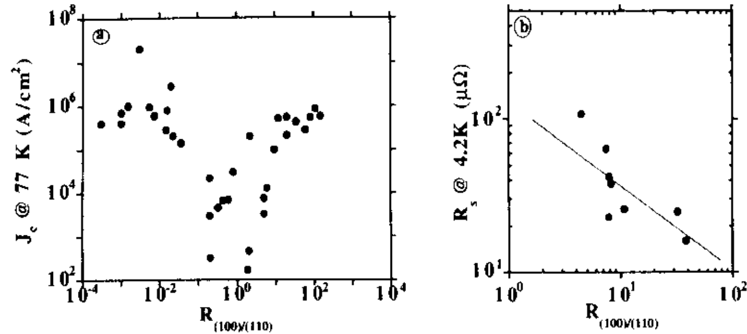

Figure 1. Critical current density, J_c, (a) [1] and surface resistance at 10 GHz, R_S, (b) [2] as a function of the in-plane orientation ($R_{100/110}$) of YBCO thin film grains.

J_c is strongly depressed in thin films with random grain orientation (R≈1), where many large angle grain boundary are present; best J_c and R_s values were obtained for highly textured YBCO thin films. In general the best transport properties are achieved when YBCO thin film microstructure approaches that of a single crystal, that is when large grains with low angle grain boundaries and low defect density are produced.

In this example, as in many other regarding thin films for electronic devices, high quality thin films were obtained by finely optimising the deposition process and by a careful selection of the substrate materials. In fact, the choice of a suitable substrate is largely responsible for the microstructure, especially when the correct epitaxial relationship is established between substrate and thin film. Therefore, substrate properties are also to be considered and besides material choice and control of surface quality, also the real crystallographic orientation of single crystal substrates must be tested. Considering again YBCO, thin films grown on MgO substrates polished off-axis from the [001] direction showed remarkable texture change, influencing the superconducting properties. As shown in Figure 3 [3], a 4° off-axis angle led to a strong degradation of both J_c (about one order of magnitude) and T_c.

It is widely recognised that X-ray diffraction (XRD) is the most suitable analytical technique for non-disruptive structural characterisation of thin films; typically, XRD is used to study phase composition, lattice parameters and epitaxy, through texture measurements.

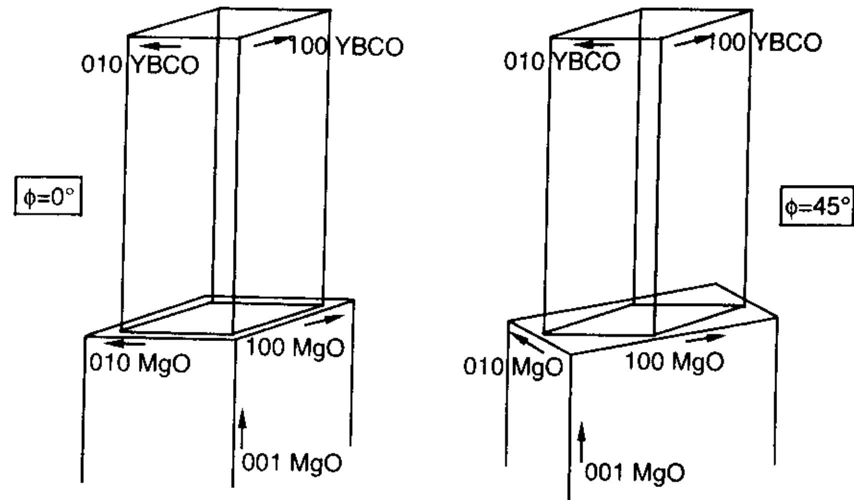

Figure 2. Definition of YBCO orientation on (100) MgO: ϕ=0°, [100] MgO ‖ [100] YBCO (or [010] YBCO) (a) and ϕ=45°[110] MgO ‖ [100] YBCO (or [010] YBCO) (b).

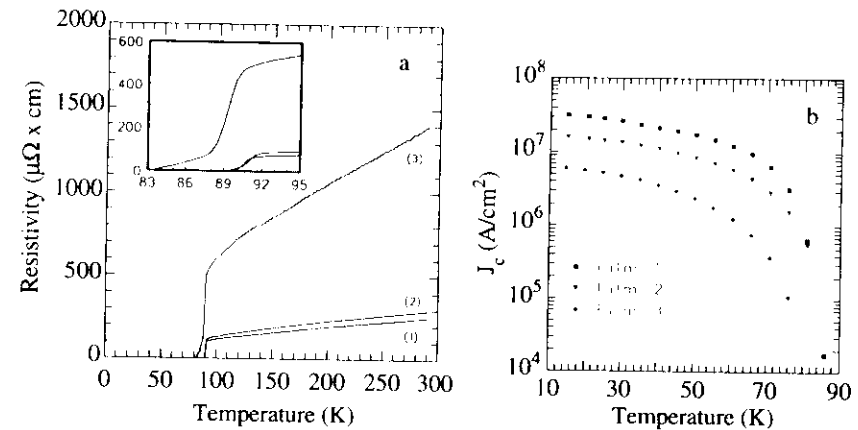

Figure 3. Resistivity (a) and critical current density (b) versus temperature for YBCO films deposited by laser ablation on (100) MgO cut at different angles off-axis: 0.80° (1), 1.23° (2) and 4.00° (3) [3].

However, even if it is largely employed in thin film studies, a great part of the information which could be obtained from XRD measurements is not usually considered.

The main reasons are essentially two: firstly, the geometrical assembly of XRD instruments frequently used in thin film studies is not always appropriate; secondly, little use is made of analytical tools already developed for X-ray powder diffraction (XRPD), probably the most diffuse application of XRD, which could be easily employed also for data processing of thin films patterns.

The present work is aimed to show some of these methods, concerning line broadening and texture measurements, which can give a detailed information on the microstructure, and can be easily used with XRD instruments employing traditional geometry [4-6]. In particular, after a short description of the most diffuse geometrical set-ups appropriate for thin film studies, two different systems will be considered: (a) YBCO thin films deposited on single crystal substrates, with or without thin buffer layers, characterised by a high texture and columnar grain shape due to epitaxial growth; (b) CaO-stabilised zirconia (CaSZ) on Si wafers, with low texture and complex grain size and shape distribution. In both cases, texture will be studied by traditional Bragg-Brentano (BB) patterns and by using specific techniques like Ω-scans and pole figures, whereas line broadening analysis of BB patterns will be used to find the distribution of crystallite size and microstrain, which is directly connected to lattice disorder.

2. Experimental methods

XRD of thin films can be carried out using several instruments with different geometry;

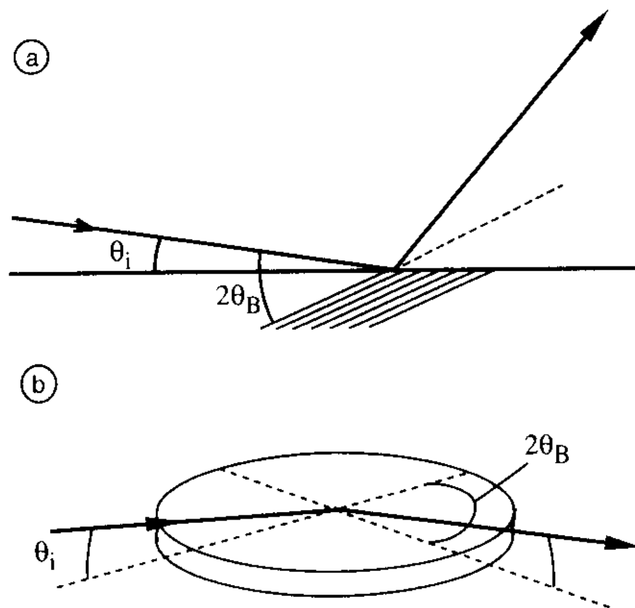

Figure 4. GID geometry. Asymmetrical (a) and symmetrical (b).

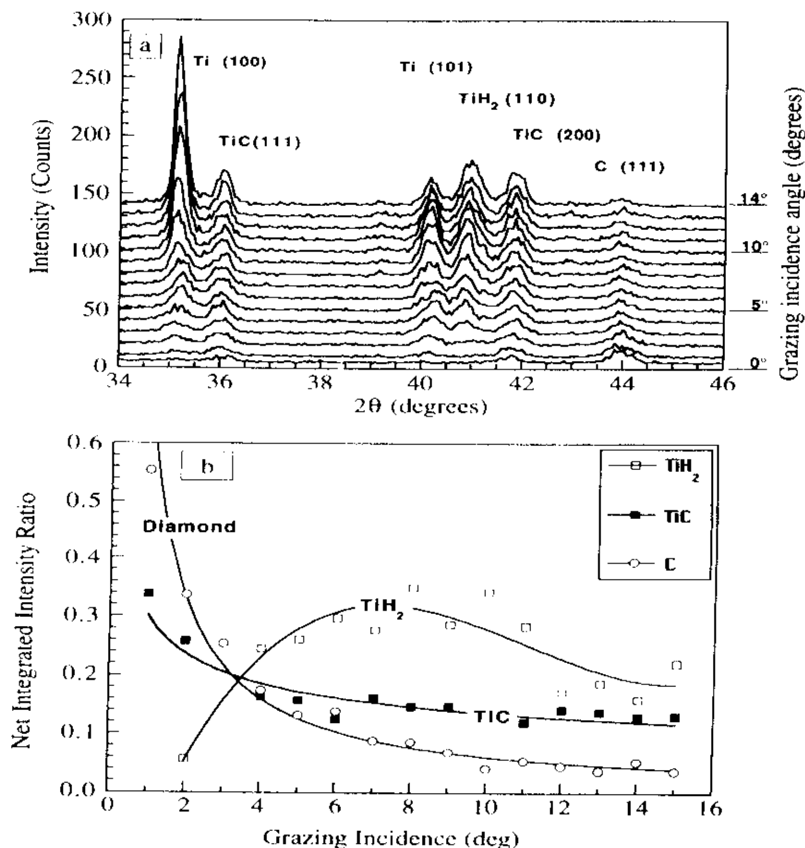

Figure 5. GID patterns of a diamond film on Ti alloy (a). Semi-quantitative phase composition plot (b) [12]

some of them have been purposely designed, like the Seeman-Bohlin (SB) [7,8], in order to increase the signal diffracted from the thin film and to reduce or even eliminate that from the substrate. As the present work is limited to XRD with traditional equipment, the reader can refer to cited literature for further details on instruments specific for thin film XRD [7-11]; though, it must be underlined that unlike SB, which generally needs a dedicated instrument, grazing incidence diffraction (GID) measurements can be carried out also by traditional diffractometers with suitable set-up. Figure 4 shows the geometry of symmetrical and asymmetrical GID [10-11].

An important feature of SB and GID techniques is the possibility of changing the depth of the studied thin film region, by varying the incidence angle; in this way depth profiling of important structural parameters like residual stress, lattice constants or phase composition can be obtained. On the other hand, it must be recognised that it can be difficult to make GID measurements in the presence of high texture and/or surface roughness.

As an example of the application of this technique, Figure 5 shows several asymmetrical GID patterns from a diamond thin film deposited on a Ti alloy by CVD [12]. Phase analysis by traditional XRD in BB geometry led to the identification of TiC and TiH_2 besides diamond; even though multilayer structures can be studied by using BB patterns [13,14], in this case the low absorption of diamond made it difficult to understand the spatial distribution of phases. On the contrary, from GID patterns of Figure 5 it can be seen that at low incidence angle only C peaks are present, while TiC and TiH_2 signals increase at higher angle: this sequence suggests that diamond is in the top layer, whereas Ti compounds formed at the interface with the Ti alloy, whose signal is present only above $a \sim 1°$. As shown in Figure 5b, a semi-quantitative analysis of phase composition can be obtained by comparing integrated intensity (area) of peaks from the identified phases [12].

Figure 6 shows schematically the geometry of a Bragg-Brentano diffractometer. This

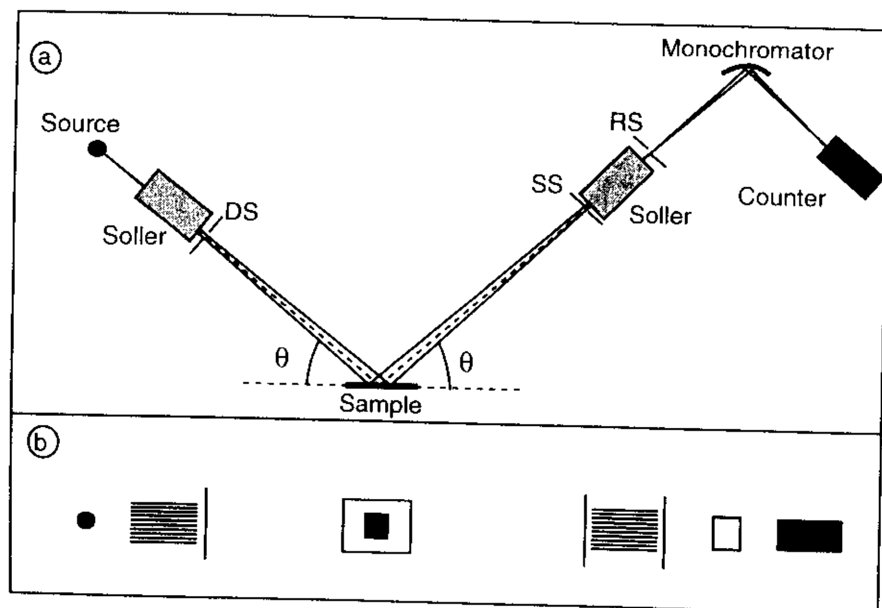

Figure 6. Bragg Brentano geometry: top (a) and side (b) view. Soller, Divergence (DS), Antiscattering (SS) and Receiving (RS) slits are indicated

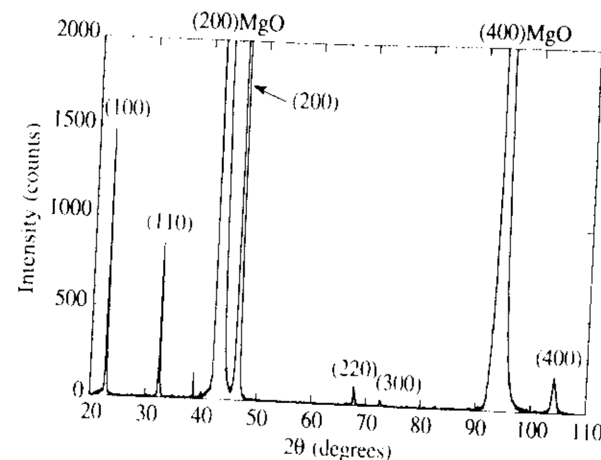

Figure 7. XRD pattern in Bragg-Brentano geometry of a 53 nm $SrTiO_3$ film on (100) MgO. Miller indexes are reported for all identified peaks. Unmarked peak at ~38° is a kβ reflection of (200) MgO.

configuration is used extensively for XRPD studies, but it can be used with success also for thin films. One of the limits is the thickness of the studied layer; the minimum thickness which can be analysed depends on the absorption of the material, but it is also influenced by the texture. Highly textured thin films concentrate all the diffracted intensity in one or a few Bragg peaks, which can be quite intense also for very thin films. As shown in Figure 7, the BB pattern of a 53 nm film of $SrTiO_3$ on MgO is clearly visible and rich of details; two different sets of grains are present with (h00) and (hh0) planes, respectively, parallel to the surface, and up to the fourth (h00) diffraction order is observed (counting time 5 s, step 0.05°, 40kV/45mA).

The limits of resolution in this configuration are usually found when studying thin nanocrystalline or amorphous materials, which can be practically transparent to the X-ray beam. Anyway, the transparency of the thin films is not always a drawback for BB analysis; in fact, the partial absorption of the beam can be used to calculate the thickness in multilayer coatings, provided that texture is not to high and absorption not too low [13,14].

One of the advantages of BB diffractometers is the possibility of analysing a wide class of polycrystalline materials, giving XRD patterns with well resolved profiles. In fact, the parafocusing geometry (Figure 6a) can give narrow, intense and well-shaped Bragg's peaks which is a necessary requirement for many types of analysis. In particular, by using narrow DS/RS and Soller slits it is possible to reduce equatorial and axial divergence, respectively, so to obtain very narrow and symmetrical profiles [15]. A further improvement can be achieved by the use of a monochromator (preferably in the diffracted

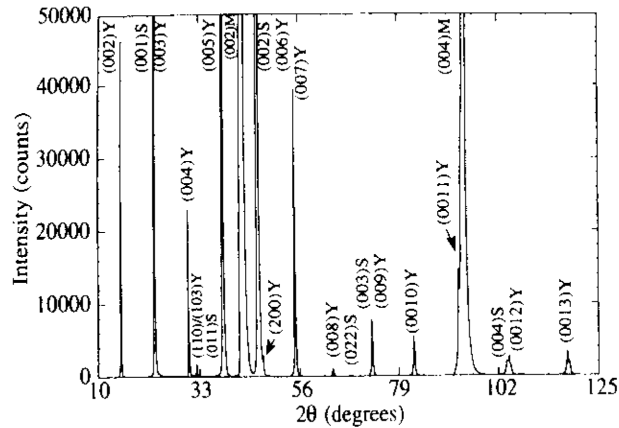

Figure 8. XRD pattern of a 200 nm YBCO film deposited on the sample of Figure 7. Miller's indexes of MgO (M), $SrTiO_3$ (S) and YBCO (Y) phases are reported [6].

beam, so to cut possible fluorescence from the sample), which adds a further limitation of the axial divergence and above all leads to a very high signal to noise ratio, reducing the background signal down to few counts per second (cps). Under such conditions a high resolution can be obtained, approaching that of an XRD station of a synchrotron radiation source [16]; on the other hand, it must be considered that counting time is considerably increased. As shown in the next paragraph, this high resolution BB geometry is the most suitable for reliable profile modelling and LBA.

Part of the information concerning thin film texture can be obtained from BB patterns; in fact, BB geometry is such to bring in diffraction condition only those grains whose atomic planes in Bragg's condition are parallel to the surface of the sample (Figure 6).

Therefore, it is generally possible from BB patterns to have a qualitative picture of the texture, which is frequently sufficient to estimate the degree of epitaxy of a thin film. As shown in Figure 8, the pattern of a 200 nm YBCO film [6], grown on a (100) MgO substrate with the $SrTiO_3$ buffer of Figure 7, shows several 00*l* peaks of YBCO orthorhombic structure which suggest a c⊥ growth with respect to the substrate/buffer system, whose reflections are also visible. The presence of weak (h00) and (110)/(103) YBCO reflections indicates that a small fraction of grains grew along different orientations.

As will be described later, using a BB diffractometer further information can be obtained on the mosaic spread of the c⊥ oriented grains, which can be measured by the rocking curve. The limit of BB measurements is that nothing can be said about the in-plane orientations. To have a complete picture of the texture it is necessary to investigate how the

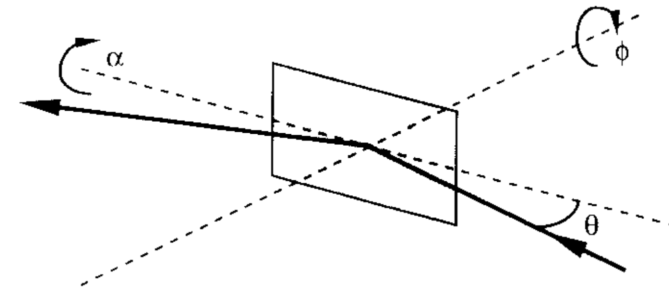

Figure 9. Definition of angles in pole figure measurements.

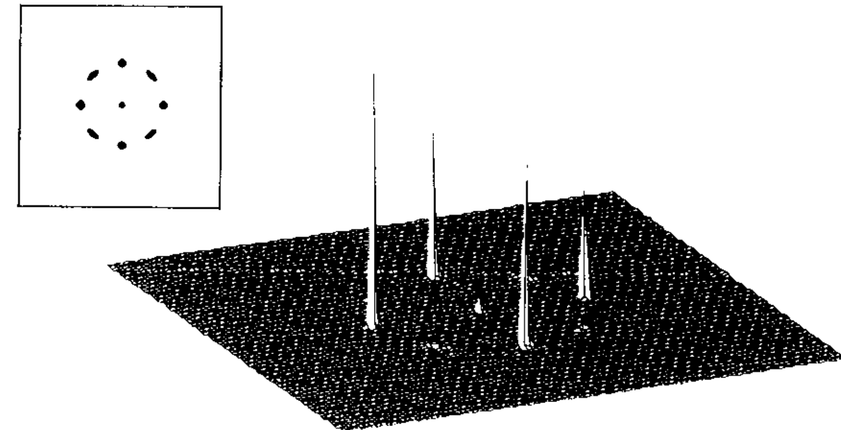

Figure 10. (110) $SrTiO_3$ pole figure of the sample of Figure 7; the inset shows the contour map [6].

intensity diffracted from several Bragg's reflections is distributed as a function of the beam incidence angle. This is the principle of pole figure measurements, whose rotation angles are defined in Figure 9. After a Bragg's peak (pole) has been chosen, the counter is positioned to the 2θ value corresponding to peak maximum; then, the diffracted signal is measured for each couple of angles (α,ϕ) describing the orientation of the sample surface with respect to the incident beam. Unlike BB diffractometers, the X-ray beam cannot be divergent since the parafocusing condition (Figure 6a) cannot be preserved when the

incidence angle is different from the reflection angle. In pole figure measurements a parallel beam is used, which is produced with suitable collimators and a monochromator with flat rather then curved crystal.

The presence of a monochromator, as in the BB geometry, is very important to increase the quality of the signal and to avoid artefacts due to the continuous radiation emitted by the X-ray source [17].

Figure 10 shows the (110) $SrTiO_3$ pole figure relevant to the sample of Figure 7. The pole in the centre is due to grains grown along [001] MgO ‖ [011] $SrTiO_3$, whereas the four intense poles at α=45° and ϕ=0, 90, 180, 270° correspond to the large fraction of grains grown along [001] MgO ‖ [001] $SrTiO_3$, with [100] MgO ‖ [100] $SrTiO_3$ (cube on cube).

This observation is clearly in agreement with the BB pattern, but further information is given by the pole figure which is not contained in Figure 7; in fact, four weak poles are present at α=45° and ϕ=45, 135, 225, 315° (see inset of Figure 11), which are due to grains grown along [001] MgO ‖ [001] $SrTiO_3$, but with [100] MgO ‖ [110] $SrTiO_3$. As shown by Figure 1, this information on in-plane orientation is particularly important when studying the properties of epitaxial thin films.

It is a common practice to make Ω-scans (or ϕ-scans) to study in-plane orientations [1-3,18,19]; these measurements are conducted by measuring pole intensity during a scansion of ϕ angle, while α is kept constant (see Figure 9). Figure 11 shows the ϕ-scan for the sample of Figures 7 and 10; the measurement was performed on the (110) $SrTiO_3$ pole, and a fixed value of α=45° was set, so that the in-plane orientation of $SrTiO_3$ grains grown along [001] MgO ‖ [001] $SrTiO_3$ was measured. Basically, the ϕ-scan of Figure 11

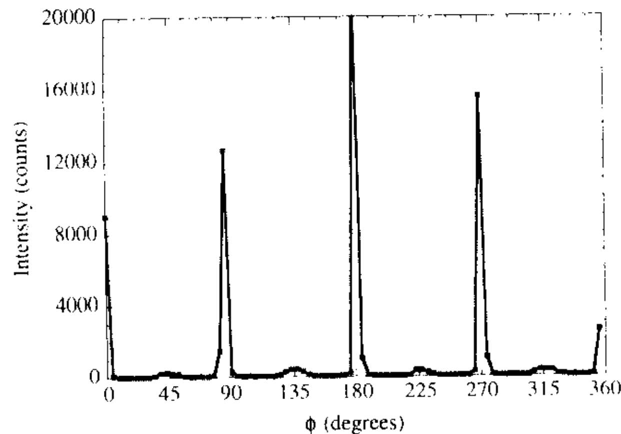

Figure 11. ϕ-scan of the sample of Figures 7 and 10. The (110) $SrTiO_3$ pole was measured with fixed α=45°.

corresponds to a circle at α=45° in the (110) $SrTiO_3$ pole figure (Figure 10); the main advantage is that it takes much less time to make a ϕ-scan than a pole figure, but it is worth noting that the information from a ϕ-scan is not complete. More or less large fractions of grains can be oriented in such a way to be undetected by ϕ-scans; concerning the present example, this is true for the small fraction of grains grown along [001] MgO ‖ [011] $SrTiO_3$, but unobserved poles may be much stronger, as shown later for YBCO thin films. Therefore, ϕ-scan is a useful analytical tool, but the results must be evaluated carefully, to avoid that only part of the information regarding the texture is considered.

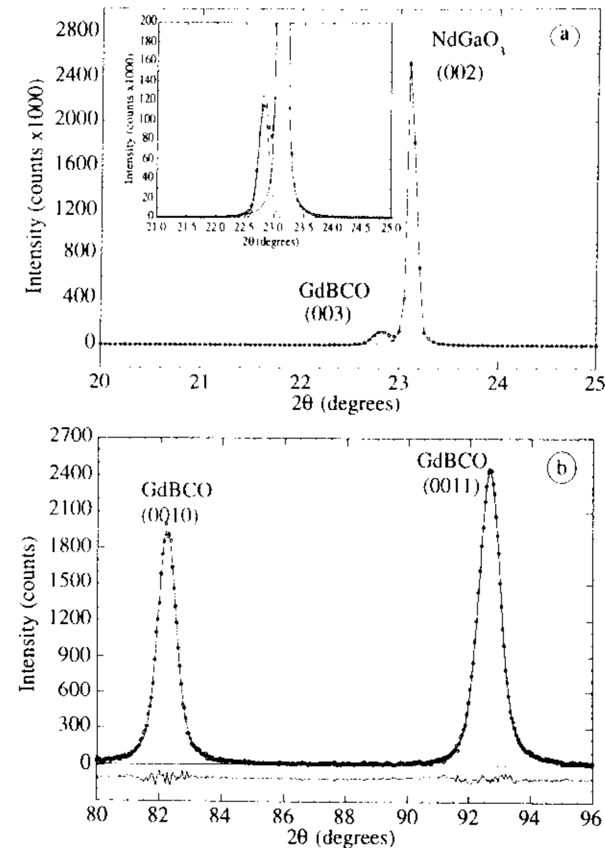

Figure 12. XRD patterns of $GdBa_2Cu_3O_{7-\delta}$ (GdBCO) on $NdGaO_3$ single crystal substrate. Experimental (dot) and modelled (line) profiles are reported along with the residual (difference between experimental and modelled)

In the present work two basically different diffractometers where used for (1) LBA and (2) texture measurements: (1) Rigaku PMG-VH with 1/2° (DS), 1/2° (SS), 0.15 mm (RS), 2° (Soller) and a graphite curved crystal monochromator in the diffracted beam; (2) Huber 4030 Stress/Texture with 4-circle goniometer and graphite flat crystal in the diffracted beam.

3. Line Broadening Analysis (LBA).

XRD Line Broadening Analysis (LBA) is a well-known technique to study crystallite size distribution and lattice disorder in powder samples and, in general, polycrystalline materials. Initially developed to study lattice disorder in metals [20-24], LBA is frequently used in materials science, mainly for powder and bulk samples. Even though there is no actual restriction, its use to study thin films, especially when highly textured, is much less frequent. Paradoxically, since most reliable LBA methods need two or more diffraction orders of the same crystallographic plane family, textured films are particularly suited to be analysed by this technique.

A detailed treatment of this subject is beyond the scope of this work, therefore only a brief description of the used method is given here; further details may be found in the cited literature [20,21,24,25]. LBA was carried out by the Warren-Averbach (WA) method [20,21], appropriately modified to permit the application of analytical profile modelling [26-28]. Profile fitting is extremely effective and useful to speed up calculations and reduce errors arising from the necessary Fourier analysis; moreover, profile fitting is absolutely necessary to solve problems due to peak overlapping, which are frequently met studying polyphasic samples and low symmetry materials, and when profiles are very broad.

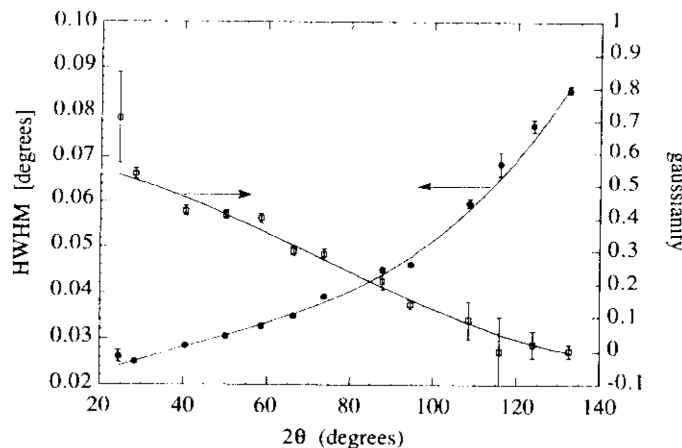

Figure 13. Half Width at Half Maximum (HWHM) and gaussianity (η) as a function of 2θ. Standard KCl powder sample.

Several analytical functions have been proposed to model XRD peaks; pseudo-Voigt (pV) functions are a good approximation of real profiles and are easy to handle analytically, since they are simply defined as a linear combination of a Gauss and a Cauchy curve:

$$pV(2\theta) = \sum_{\alpha_1,\alpha_2,\alpha_{3,4}} I_0 \cdot \left[\frac{1-\eta}{1+S^2} + \eta \cdot \exp\left(-\ln 2 \cdot S^2\right)\right] \quad (1)$$

$$S = (2\theta - 2\theta_B)/HWHM \quad (2)$$

where I_0 is the intensity, HWHM is the Half Width at Half Maximum, η is the gaussianity and θ_B is the position of the maximum of a Bragg's peak; each XRD peak is described by three pV functions ($k\alpha_1$, $k\alpha_2$ and $k\alpha_{3,4}$), whereas the background can be modelled by a straight line or a polynomial function; it may appear that a huge number of parameters is necessary to model a single profile, but all those describing $k\alpha_2$ and $k\alpha_{3,4}$ are usually bound to those of $k\alpha_1$, so that free fitting parameters are four for each XRD peak. Profile fitting is carried out through a program of non-linear least squares, which can run on a PC [29]. It is worth noting that, besides a correct profile modelling necessary to LBA, better peak position and integrated intensity can be obtained in this way, also for heavily overlapped peaks, as shown in Figure 12.

A correct description of the instrumental broadening is of paramount importance for LBA; the instrumental profile depends largely on the geometry of the diffraction experiment, but it is also determined by some sample properties, such as its absorption coefficient, for instance. As described in the previous section, the set-up of a BB diffractometer is critical to obtain symmetrical and narrow profiles. The instrumental broadening can be measured on a suitable standard sample [15], virtually free of defects and with crystallites whose size is beyond any broadening effect; through profile modelling of the standard pattern, the instrumental broadening can be parametrized in terms of peak position, HWHM and η as shown in Figure 13.

Measured XRD profile, h(ε), is a convolution of a "pure" diffraction profile, f(ε), due to crystallite size and lattice disorder, with the instrumental profile, g(ε):

$$h(\varepsilon) = \int g(\eta) \cdot f(\varepsilon - \eta) \cdot d\eta \quad (3)$$

After the measured profile h(ε) has been modelled analytically and g(ε) is known as described in Figure 13, the deconvolution of the instrumental broadening can be easily obtained through Fourier Transform (FT) [30,25]:

$$F(\varsigma) = \frac{H(\varsigma)}{G(\varsigma)} \quad (4)$$

where F(ζ), H(ζ) and G(ζ) are the Fourier coefficients of the analytical FT of the pV functions modelling f(ε), h(ε) and g(ε), respectively. This procedure is extremely advantageous with respect to numerical FT [26,27,31] and gives in analytical form the cosine Fourier coefficients of the XRD profile, A_n, corrected for instrumental broadening, which are the input data for the WA procedure. In fact, it can be shown that [25]:

$$A_n = A_n^S \cdot A_n^D \quad (5)$$

where A_n^S and A_n^D are the broadening components due to size effect and lattice distortion, respectively, and n is the harmonic number.

In the WA model, the material is divided in crystallites, each one diffracting incoherently from the others; crystallites are made of columns of cells along a given [hkl] direction, whose length is proportional to the interplanar distance, d_{hkl}, which is the height of a single cell. Therefore, we may define a correlation distance between two cells as $L = n \cdot d_{hkl}$, which is the distance between two cells n times d_{hkl} apart.

The two broadening components can be separated by a logarithmic relation, which can be written as:

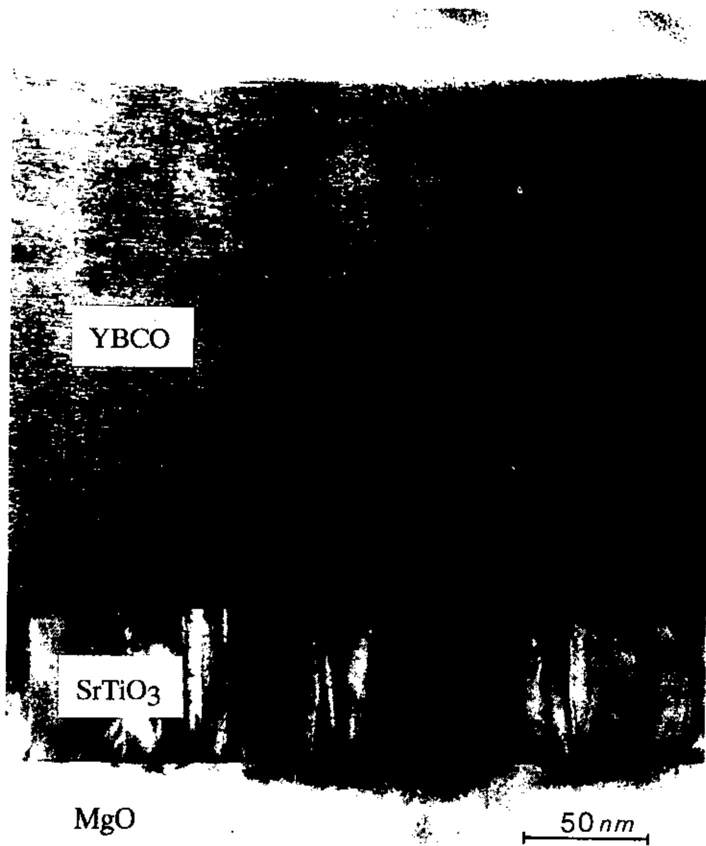

Figure 14. TEM picture of the YBCO/$SrTiO_3$/MgO cross-sectioned sample of Figure 8. (Courtesy of A. Migliori)

$$\ln A_L(d_{hkl}) = \ln A_L^S - \frac{2\pi^2 \cdot \langle \varepsilon^2(L) \rangle \cdot L^2}{d_{hkl}^2} \quad (6)$$

where $\langle \varepsilon^2(L) \rangle^{1/2}$ is the microstrain, expressing lattice distortion [5,26-28]. Using two or more reflection orders (e.g., (001) and (002)), it is possible to calculate A_L^S and $\langle \varepsilon^2(L) \rangle$ from a plot of $\ln A_L(d_{hkl})$ versus $1/d_{hkl}^2$. Moreover, it can be shown that the mean column length, $\overline{M}$, along [hkl] is given by

$$\left. \frac{dA_L^S}{dL} \right|_{L \to 0} = -\frac{1}{\overline{M}} \quad (7)$$

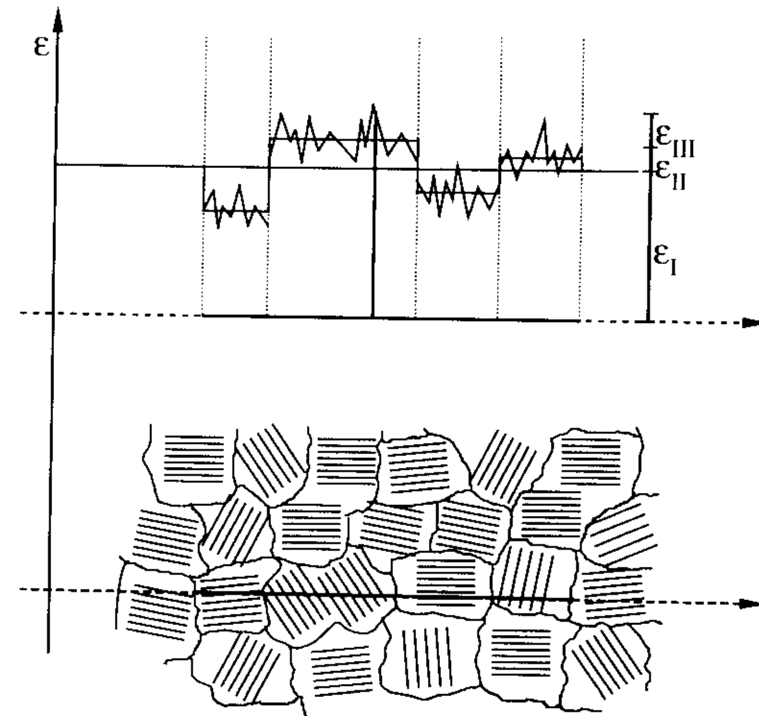

Figure 15. Residual strain inside a polycrystalline material.

$\overline{M}$ is also referred to as the mean crystallite size, even though, strictly speaking it is the average length of the columns of cells composing crystallites, along [hkl]; therefore, the

connection to the actual grain size is not straightforward, and depends strongly on the shape of crystalline domains [32-34]. Concerning this point, the meaning of LBA of powder patterns may be different from that of thin film patterns. In a powder and in many polycrystalline bulk samples it is supposed that grain orientation is random, and frequently the morphology of grains is quite heterogeneous; two different Bragg's reflections may be produced by grains absolutely equivalent, which differ only for their orientation with respect to the beam.

On the contrary, thin film often exhibits columnar grains with strong texture due to growth mechanism and epitaxial relationship with substrate structure. For instance, Figure 14 shows a TEM picture of a $YBCO/SrTiO_3/MgO$ cross-sectioned sample like that of Figure 8, where the columnar grain shape can be seen both in the buffer and in the superconducting layer. In a textured thin film each hkl peak comes from a distinct set of grains with a given epitaxy, such that grains grew with (hkl) planes parallel to the surface; therefore, two Bragg's peak from different planes (e.g., 100 and 110 in Figure 7) are due to two sets of grains with completely different orientation.

The microstrain term accounts for the lattice distortion component along the studied [hkl] direction; in particular, it represents the fluctuation of the strain field to atomic level, due to the distribution of defects and inhomogeneity. Besides microstrain, bulk materials and thin films may be subjected to residual macrostrain; in thin films this strain may be very high because of the constraints produced at the film/substrate interface, causing huge residual stress values; stress up to several GPa have been measured in thin films [35-38], which can be absolutely beyond the mechanical resistance of the relevant bulk materials.

In order to understand the meaning of micro and macrostrain, we can refer to Figure 15, where is sketched the microstructure of a generic material. The residual strain to microscopic level, may be considered as made of three terms: ε_I, is the residual macrostrain, which corresponds to the average value over a macroscopic region; the macrostrain causes an average change of d_{hkl}, which corresponds to a shift of Bragg's reflections, that can be measured accurately by XRD [39]. ε_{II} and ε_{III} are the average value on a single grain and the strain fluctuation inside a grain, respectively; therefore, ε_{II} and ε_{III} represent the fluctuation of the strain with respect to the mean value, which we called microstrain. It is worth noting that the definition of microstrain, $<\varepsilon^2(L)>^{1/2}$, is correct for powder samples, were $<\varepsilon(L)>=0$; in general, for bulk and thin films, where a mean strain component may be present, the microstrain is correctly defined as

$$\sqrt{<\varepsilon^2(L)> - <\varepsilon(L)>^2} \tag{8}$$

However, for simplicity we refer to $<\varepsilon^2(L)>^{1/2}$, even if it is implicitly assumed the definition of Eq. 8.

Several types of structural defects may be present in thin films, and many of them have a marked effect on XRD profile width and shape, like atomic substitutions and vacancies, dislocations, stacking and twin faults. When faulting is present, the mean column length defined by Eq. 7 is an effective value, $\overline{M}_{eff}$, which also contains information on faulting; the real mean size, $\overline{M}_{av}$, is bigger and is given by:

$$\frac{1}{\overline{M}_{eff}} = \frac{1}{\overline{M}_{av}} + \frac{1}{\overline{M}_{sf}} \tag{9}$$

where $\overline{M}_{sf}$ is the component due to faulting. Unfortunately, the effects of faulting are difficult to be measured in thin films for several reasons: (a) stacking, deformation and twin faults measurements from XRD patterns [24,25] are usually conducted on metal and alloys and a few oxides [40] with cubic or hexagonal symmetry. No theory is available at present for lower symmetry. Therefore, no correct method is known for HTc superconductors with pseudo-perovskite structure (e.g., YBCO is orthorhombic); (b) thin films may be subjected to strain or compositional gradients which can produce similar effect on XRD profiles as faults; (3) finally, textured films like YBCO in Figure 8, give only reflections from one plane family ((00*l*) in Figure 8); this makes it impossible to apply traditional methods for stacking fault probability calculation, which partly base on peak shift of neighbouring pairs of reflections. In summary, it is important to underline that Eq. (7) gives an effective crystallite size value, which incorporates possible faulting effects; therefore, great care must be used when comparing results of LBA with those from other techniques, such as electron microscopy.

The WA analysis can be further carried out to have a more detailed information than mean values; in fact, it can be demonstrated that the second derivative of A_L^S is proportional to the distribution function of the column length probability along [hkl] [25]; this crystallite size distribution, $p(L)$, together with the microstrain distribution, $<\varepsilon^2(L)>^{1/2}$, is shown in Figure 16 for the $SrTiO_3$ sample of Figure 7, along [hh0] direction.

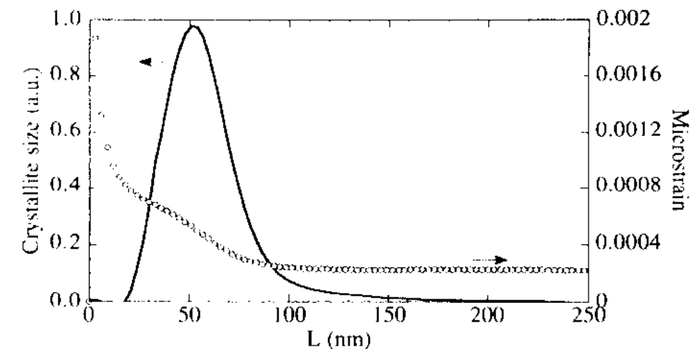

Figure 16. Crystallite size and microstrain distributions along [hh0] ($SrTiO_3$ thin film of Figure 7).

Even though details of these distributions are not always reliable [41,42], mean value and width of $p(L)$ are generally meaningful, whereas further information on the nature of

the lattice disorder can be obtained from the trend of $<\varepsilon^2(L)>^{1/2}$ [43-44]. The mean microstrain value [45-46] is usually calculated at $L=\overline{M}/2$, even if this choice is somewhat arbitrary. Therefore it is suggested to use the mean value weighted on the size distribution $p(L)$:

$$<<\varepsilon^2(L)>^{1/2}>=\frac{\int<\varepsilon^2(L)>^{1/2}\cdot p(L)\cdot dL}{\int p(L)\cdot dL} \quad (10)$$

In the following, both $<\varepsilon^2(L)>^{1/2}_{\overline{M}/2}$ and $<<\varepsilon^2(L)>^{1/2}>$ will be reported.

The mechanism causing microstrain can be investigated by the Vogel-Haase-Hosemann (VHH) method [47], which considers the logarithm of the ratio between Fourier coefficients of two peaks from the same (hkl) plane family:

$$\ln\left[\frac{A_L(h)}{A_L(h+1)}\right]\propto L^2\cdot<\varepsilon^2(L)> \quad (11)$$

where h is the diffraction order. The trend of $<\varepsilon^2(L)>$, obtained from a $\ln[A_L(h)/A_L(h+1)]$ vs. L plot, can be attributed to several disorder mechanisms. In particular, microstrain associated to dislocations gives $<\varepsilon^2(L)>\propto 1/L$, which corresponds to a linear VHH plot; on the other hand, an intercrystalline disorder, like a compositional fluctuation between crystalline domains, causes a microstrain independent of L ($<\varepsilon^2(L)>\approx$ constant), which gives a parabolic VHH plot. However, the effectiveness of this procedure must not be overestimated, since the interpretation of the VHH plot is not univocal; in fact, more than one type of defect may be present in a thin film, and give similar trends of $<\varepsilon^2(L)>$. An example of application of this method will be discussed in the next paragraph.

4. Results and Discussion

4.1 YBCO thin films on MgO and Al_2O_3 single crystal substrates

Since the discovery of HTc superconductors [48], researchers have been engaged in the preparation of thin films, but attempts were not immediately successful. So far HTc thin films are produced, depending on employed deposition techniques and substrates, with a wide variability of superconducting properties, as also shown in Figure 1 and 3.

Differently from traditional superconductors, the microstructure of thin films of HTc superconducting oxides has a marked influence on superconductivity, essentially for two reasons. First of all, ceramic superconductors have short coherence length (ξ cc 0.4-3 nm for YBCO), so defects, mainly grain boundary, have a deep influence; in fact, high angle grain boundaries act as weak links which depress superconducting properties. The second reasons, which is connected to the first one, is that the microstructure of a ceramic material like YBCO or Bi- and Tl-based compounds is intrinsically more complex: HTc superconductors are polyatomic oxides, with crystal symmetry lower than that of typical

metallic superconductors, and exhibit polymorphic phases; moreover, they have complex phase diagrams with several stable compounds [49], which are not all supeconductuctors.

YBCO thin films, for instance, are usually produced in the tetragonal $YBa_2Cu_3O_6$ form at high temperature, which transforms to YBCO after annealing at 400-500°C in Oxygen rich atmosphere; however, YBCO thin films do not form if produced directly in a high Oxygen pressure, since in this condition the tetragonal phase do not form [49]. Besides $YBa_2Cu_3O_{7-\delta}$ (123), other polytypoidical variants may be produced, like 223, 224 or 124, and, depending on stoichiometry, secondary phases like Y_2O_3, Cu_2O and $Y_2Cu_2O_5$ may be produced [50]. Moreover, amorphous layers may also be created, especially at the interface with substrates, under non-optimal deposition conditions [50]. The situation is even more complicate for Bi- and Tl-based compounds [49].

Therefore thin film growth is more difficult to control, and is deeply influenced by many factors regarding deposition techniques and substrates; while the microstructure of a metallic superconductor may be made as perfect as possible, close to that of a single crystal, this is much more difficult for ceramic superconductors. Hence the importance to control both orientation and size of grains, and the presence of compositional and structural defects.

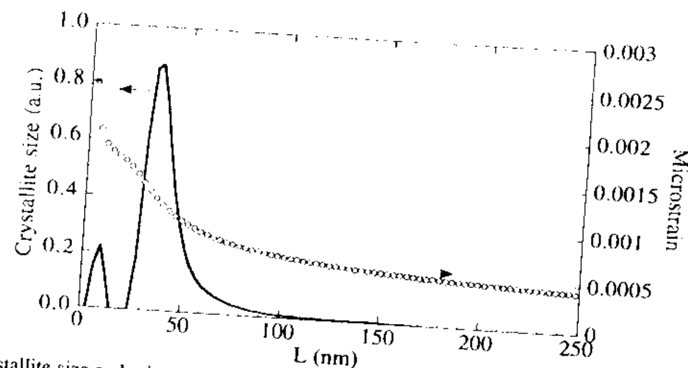

Figure 17. Crystallite size and microstrain distribution along [h00]. ($SrTiO_3$ thin film of Figure 7 and 16)

The quality of buffer layers is as much important as that of the superconductor; these intermediate layers are used as diffusion barriers to prevent from possible contamination due to substrates, but they usually work to improve the epitaxial growth of superconducting films. In the previous paragraphs it was shown the XRD of a typical buffer of $SrTiO_3$ on (100) MgO (see Figures 7, 10, 11 and 16). The main orientation was (A) [001] MgO ∥ [001] $SrTiO_3$, as shown by the BB pattern of Figure 7, but it was also present a fraction of grains (B) [001] MgO ∥ [011] $SrTiO_3$ (intensity ratio: $I_{(100)}/I_{(110)}$=169/100 with respect to 12/100 for a powder standard [51]). This result was confirmed both by (110) pole figure (Figure 10) and Ω-scan (Figure 11), which show that

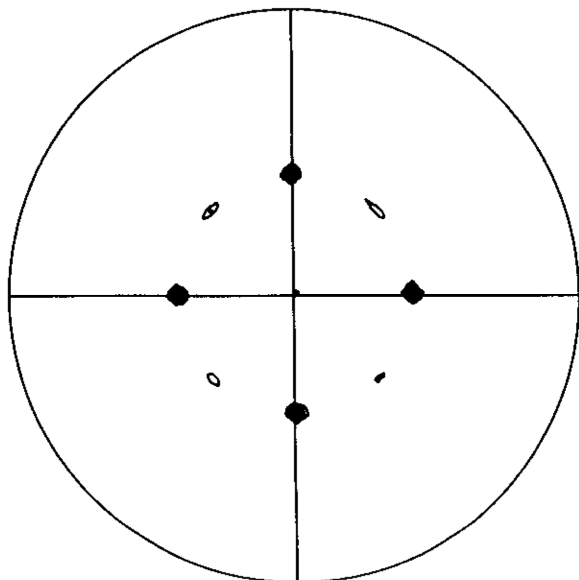

Figure 18. (103)/(013) YBCO pole figure [6].

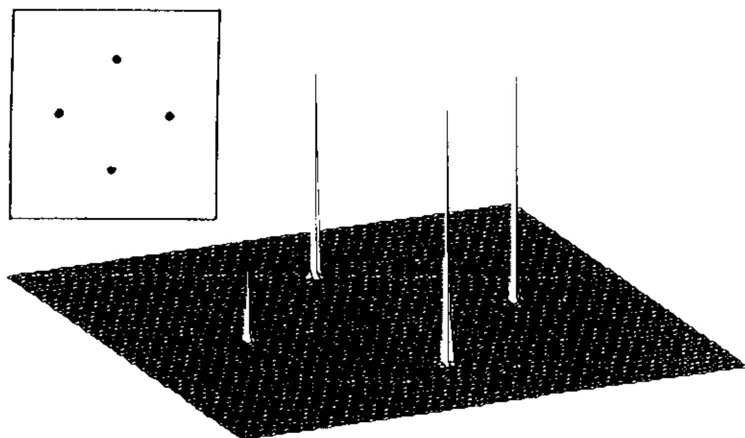

Figure 19. (102)/(012) YBCO pole figure [6]

(A) grains have a main in-plane orientation (A1) [100] MgO || [100] $SrTiO_3$, with a small fraction of twin grains (A2) [110] MgO || [100] $SrTiO_3$.

LBA showed that column length is of the order of film thickness (53 nm), confirming the high buffer quality; the column length distribution along [hh0] (Figure 16) is quite narrow, as typical of highly textured thin films [4-6], therefore we may suppose the presence of columnar grains, whose average height coincides with the average column length. This interpretation of LBA results was validated by the TEM picture of Figure 14; however, as reported in Table 1, crystallites oriented along [h00] seem to be smaller than along [hh0], probably for the presence of the two in-plane orientations (A1) and (A2); consistently, also microstrain is higher along [h00] than [hh0]. Looking at the column length distribution along [h00] (Figure 17), the presence of two groups of grains is supported by the bimodality of the distribution; we may hypothesise that the smaller grains are oriented along (A2).

Table 1. LBA results along [h00] and [hh0] for the 53 nm $SrTiO_3$ film on MgO and the 55 nm $SrTiO_3$ film on Al_2O_3.

(hkl) ⇒	100/200/300/400			110/220		
SUBSTRATE (single crystal)	$\overline{M}$ (nm)	$\langle \varepsilon^2 \rangle^{1/2}_{\overline{M}/2}$	$\langle \langle \varepsilon^2 \rangle^{1/2} \rangle$	$\overline{M}$ (nm)	$\langle \varepsilon^2 \rangle^{1/2}_{\overline{M}/2}$	$\langle \langle \varepsilon^2 \rangle^{1/2} \rangle$
MgO (100)	42	16×10^{-4}	12×10^{-4}	52	7×10^{-4}	5×10^{-4}
Al_2O_3 ($1\bar{1}02$)	22	26×10^{-4}	19×10^{-4}	53	9×10^{-4}	4×10^{-4}

The presence of two orientations, (A) and (B), may be critical to YBCO growth; the main epitaxial relationship is between planes $\{00l\}SrTiO_3$ and $\{003l\}$YBCO (c⊥), but also between $\{0ll\}SrTiO_3$ and $\{l03l\}/\{0l3l\}$YBCO. Moreover, the growth may also take place along a or b axis (a⊥ and b⊥, respectively), depending on the growth kinetics [52]. As shown is Figure 8, YBCO grew prevalently c⊥, even if BB pattern shows weak (110)/(103)YBCO and (200)YBCO reflections, due to small fractions of grains grown along the relevant directions. However, considering the intensity of these reflections, it may be concluded that the small (B) fraction of $SrTiO_3$ seems to have little effect on YBCO, which mainly grew along (A), that is [001] MgO || [001] $SrTiO_3$ || [001]YBCO.

As discussed regarding Figure 1, it is also very important to point out if c⊥ grains grow with $\phi=0°$ or $\phi=45°$, that is [100] MgO || [100] YBCO (or [010] YBCO) or [110] MgO || [100] YBCO (or [010] YBCO). Given the presence of (A1) and (A2) $SrTiO_3$ grains it is important to study the in-plane orientation of YBCO; typically this is done by a (103)/(013) YBCO pole figure or Ω-scan, which has an intense diffracted signal (d=2.750 Å; relative intensity, Irel=55/100 [53]) although it is not easily distinguishable from (110) YBCO (d=2.725 Å; Irel=100/100 [53]). Figure 18 shows the (103)/(013) YBCO pole figure: the main orientation is c⊥, $\phi=0°$, but it is also visible a fraction of c⊥, $\phi=45°$; unlike BB pattern,

there is a remarkable fraction grains along [001] MgO || [103] YBCO (or [013] or [110]), which produces the peak in the centre of the pole figure. Actually, this is an artefact, due to a partial overlapping with the signal diffracted by the (110)$SrTiO_3$ pole (d=2.759 Å [51]).

Thus, the real YBCO texture on perovskite substrates is better evaluated by the (102)/(012) YBCO pole figure (Figure 19); even though the relevant Bragg's reflection is less intense (d=3.235 Å, Irel=3/100 (102); d=3.196 Å, Irel=5/100 (012)), no peaks from buffer or substrate are in the vicinity. As shown in Figure 18, in spite of the presence of (A2) $SrTiO_3$ grains, YBCO grew along c⊥, ϕ=0°, probably because of a preferred nucleation of YBCO on (A1) $SrTiO_3$ grains [6]. Note that Figure 19 does not show the small part of [001] MgO || [103] YBCO (or [013] or [110]) grains which were found from BB pattern; this demonstrates the high sensitivity of the traditional BB technique.

LBA was conducted on several diffraction order from (001) YBCO planes; the column length distribution has a shape similar to that of Figure 16, but the mean size is 80 nm [6]; comparing this value with film thickness (220 nm), we may suppose that YBCO columnar grains are interrupted by planar defect, such as dislocation arrays or stacking faults [54], even though the overall microstructure is quite ordered. The quality of the film is attested by T_c=90K and $J_c=2\times10^6$ A/cm² at 77K [6].

Changing the substrate has a remarkable effect on $SrTiO_3$/YBCO microstructure. Depositing buffer and superconductor by the same technique (pulsed laser ablation (PLA)[3,6,55]) in the same conditions as used previously on MgO, but using an R-plane Al_2O_3 (sapphire) substrate, leads to completely different orientation and grain size distribution.

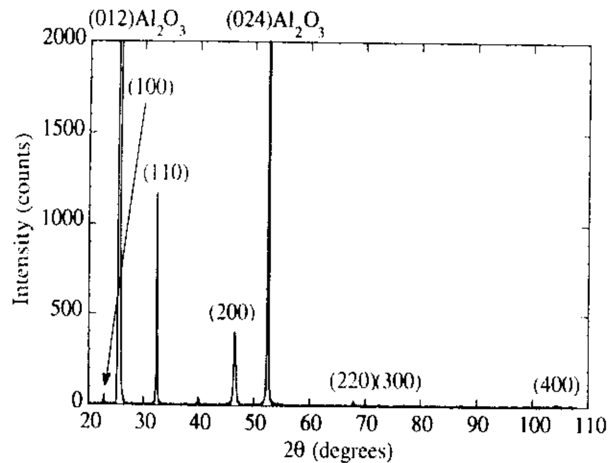

Figure 20. Bragg-Brentano pattern of a 55 nm $SrTiO_3$ film on R-plane Al_2O_3.

Figure 20 shows the BB pattern of a $SrTiO_3$ film on R-plane Al_2O_3. In this case, the film is much less textured (intensity ratio: $I_{(100)}/I_{(110)}$=6/100 with respect to 12/100 for a powder standard [51]), with a slight preferred orientation along [110]. LBA (see Table 1) confirmed that grains grown along [hh0] are defect free, and run through the whole film thickness, whereas grains along [h00] are much smaller and consequently show higher microstrain.

This result is consistent with the low orientation of $SrTiO_3$ on sapphire with respect to $SrTiO_3$ on periclase. The (110) $SrTiO_3$ pole figure (Figure 21) exhibits several poles, corresponding to the main [h00] and [hh0] (centre) orientations, and to the small fraction of [111]. Besides the low texture, which can be further appreciated by comparing Figure 21 with Figure 10, the poles of Figure 21 are broad, indicating a high mosaicity within each growth direction. In conclusion, the quality of the buffer seems poor, and a low quality YBCO film is expected to grow on it.

Figure 22 shows the (102)/(012) YBCO pole figure for the YBCO/$SrTiO_3$/Al_2O_3 sample. As for the buffer, YBCO was produced under the same PLA deposition conditions [56] employed for the YBCO/$SrTiO_3$/MgO sample. Despite the unfavourable texture of the buffer, the main growth direction is c⊥, even though several minor poles are present, originating from differently oriented grains. In addition to [001] (c⊥), also [100], [113] and [103] poles are visible. Moreover, the [001] (c⊥) poles are very broad, as found for the $SrTiO_3$ layer below. Note that in this case it is extremely important to study the texture by pole figures; a Ω-scan like that of Figure 11, in fact, would not show the presence of grains grown along [100], [113] and [103].

The high mosaicity of the buffer led to the growth of poorly oriented YBCO, whose superconducting properties were decidedly scarce, with a T_c around 50K [56]. According to texture results, LBA shows a high lattice disorder; the noticeable differences between YBCO/$SrTiO_3$/MgO and YBCO/$SrTiO_3$/Al_2O_3 samples can be appreciated in Table 2. Mean column length is much shorter and microstrain higher for the latter, confirming the presence of a less ordered microstructure. Much better results may be obtained on Al_2O_3 substrates by using CeO_2 buffers [56].

The two YBCO thin films described before exhibit remarkable microstructural differences which justify unlike superconducting behaviours. However, different superconducting properties may be found also among more homogeneous high quality

Table 2. LBA results along [001] YBCO for samples deposited by PLA on MgO [6] and Al_2O_3 single crystals, using $SrTiO_3$ buffers of Table 1.

(hkl) ⇒	(001) YBCO		
SUBSTRATE (single crystal)	$\overline{M}$ (nm)	$\langle \varepsilon^2 \rangle^{1/2}_{\overline{M}/2}$	$\langle \langle \varepsilon^2 \rangle^{1/2} \rangle$
MgO (100)	80	6.4×10^{-4}	4.7×10^{-4}
Al_2O_3 (1$\bar{1}$02)	41	18×10^{-4}	14×10^{-4}

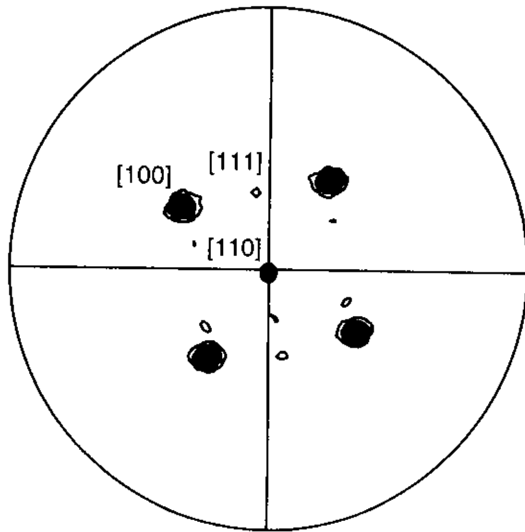

Figure 21. (110) $SrTiO_3$ pole figure of the sample deposited on R-plane sapphire

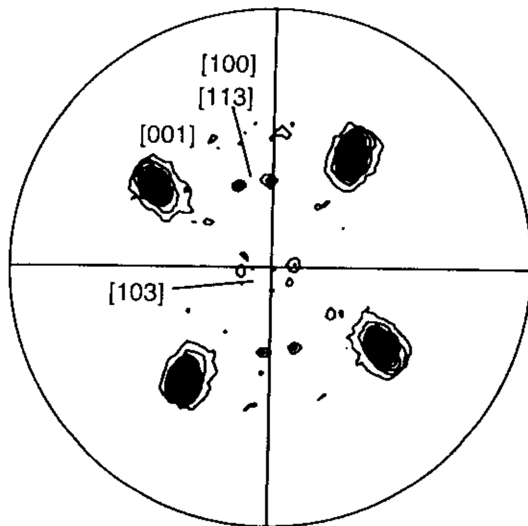

Figure 22. (102)/(012) pole figure of YBCO deposited on the $SrTiO_3$ thin film of Figure 21.

samples. Figure 23 shows part of the BB patterns of two GdBCO thin films deposited by Channel Spark Ablation (CSA) on $NdGaO_3$ single crystals [57]. Both films were c⊥, with negligible contributions from other sets of planes. As shown in Figure 24, the (102)/(012) GdBCO pole figure displays four strong poles corresponding to c⊥ (cube on cube growth of YBCO on $NdGaO_3$); the two weak poles at the same ϕ but different α value are due to a small fraction of a⊥ or b⊥ grains. In this case the BB pattern did not show clearly the relevant reflections because of the strong overlapping with substrate peaks.

The pole figures of the two samples, like the BB patterns, were equivalent. Looking for possible differences, the (005) GdBCO rocking curve was measured, by using the BB goniometer with narrow DS and RS slits (0.05 mm). As shown in Figure 25, the width of the two curves is also comparable, even if their shape is different.

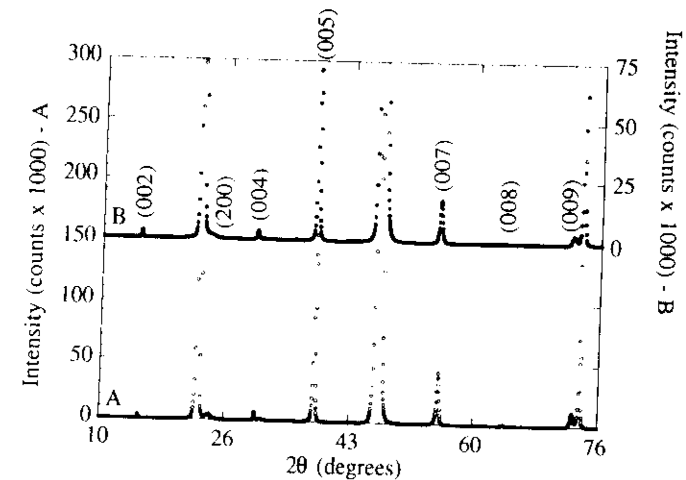

Figure 23. XRD patterns of GdBCO on $NdGaO_3$. Miller indexes of GdBCO, unmarked peaks are from the substrate. Left and right scales, A and B samples, respectively.

In spite of the similar microstructure, the two samples show different superconducting quality. Film A has T_{co}=92.6K and ΔT_c=0.9K (ΔT was defined as the temperature gap between 90% and 10% resistivity (ρ) values in the ρ vs. T curve about the superconducting transition), whereas film B has T_{co}=88.5K and ΔT_c=2.8K. These differences, rather than to texture, are due to lattice disorder, as demonstrated by LBA. As shown in Figure 26, Bragg's reflections of sample A are sensibly broader than those of film B; carrying out the LBA calculations as described before, the distributions of column length and microstrain can be calculated. From Figure 27 we may see that the mean column length of sample A is

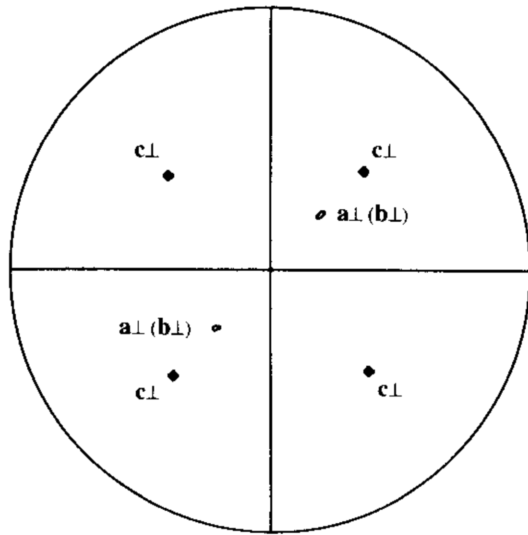

Figure 24. (102)/(012) pole figure of GdBCO deposited by CSA on $NdGaO_3$ [57].

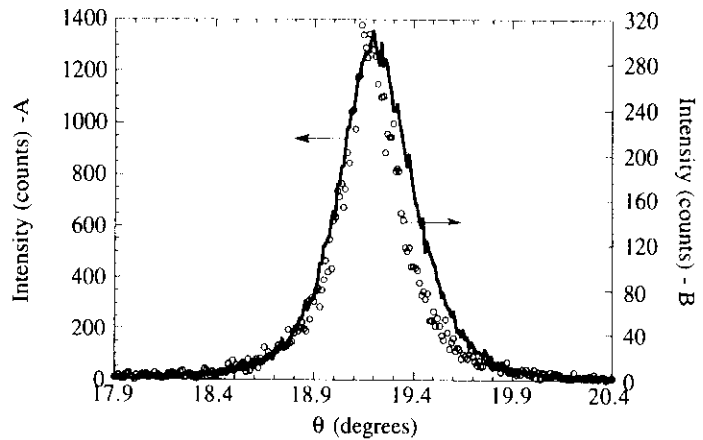

Figure 25. Rocking curves of the GdBCO thin films of Figure 23. A and B samples, line and circle, respectively.

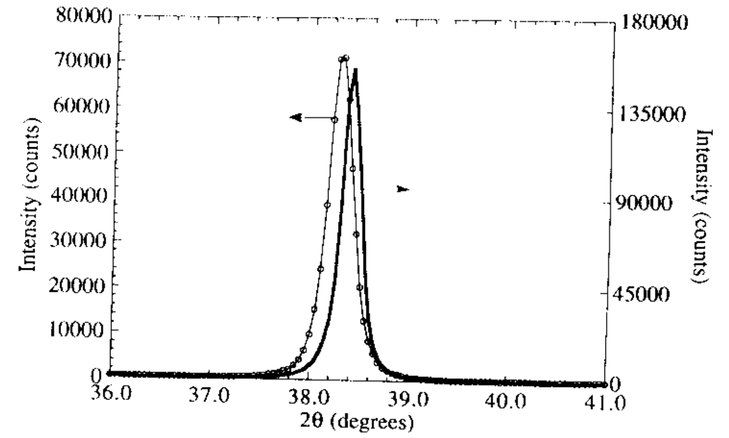

Figure 26. Comparison between (005) GdBCO reflections for sample A (line) and B (circle)

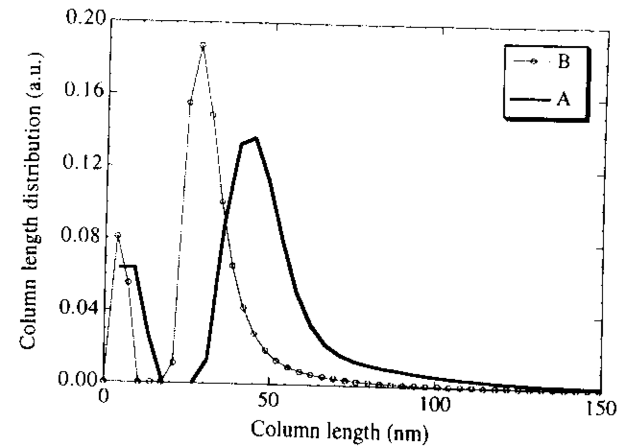

Figure 27.Column length distribution along [001] GdBCO for sample A (line) and B (circle)

longer and correspondingly microstrain lower than for sample B. From these results, considering the columnar grain structure found for these samples, we may suppose that sample B has smaller crystalline domains, leading to a worsening of the superconducting behaviour. Therefore, we may conclude that this features may be responsible for differences of T_{co} and ΔT_c (and probably J_c) among high quality samples with comparable texture [58].

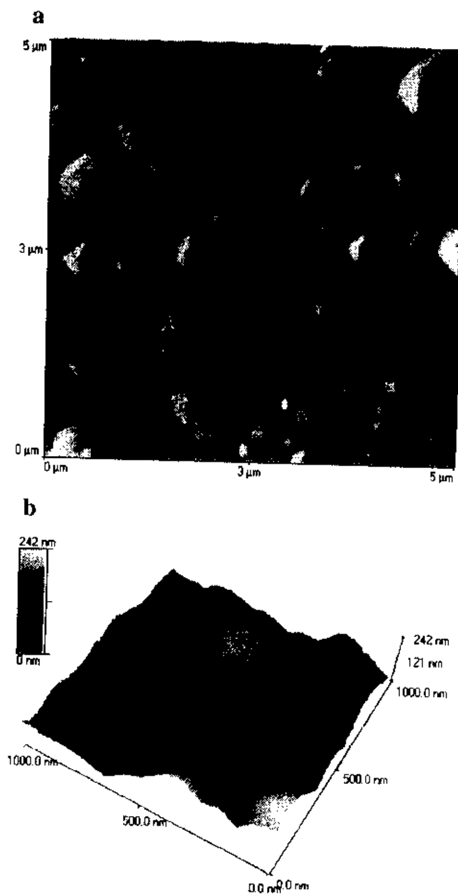

Figure 28. AFM micrograph of the surface of sample A ($GdBCO/NdGaO_3$). (Courtesy of C. Della Volpe)

The size values obtained by LBA within this context are referred to the height of grains; the size in orthogonal direction is also an interesting feature, of course. AFM (Atomic Force Microscope) measurements (Figure 28) show large particles on the surface of the samples; though, looking at a higher magnification on a single particle (Figure 28b), it can be seen that it is made of several smaller blocks whose size is around 100 nm; as explained before, this value cannot be compared with LBA crystallite size, both because referred to different directions and because of the different meaning of the two measurements; LBA gives the size of crystalline domains (including the effect of faulting), whereas AFM gives a topographic measurement. Nevertheless, as LBA crystallites and surface features observed by AFM have comparable size, we may conclude that these films are made of grains much smaller than particles observed in the low magnification picture.

4.2 *CaO-stabilised ZrO_2 thin films on <111>Si wafers*

There is a considerable interest in the production of thin films of stabilised zirconia for several electronic applications like oxygen sensors, broad band interference filters, laser mirrors, gyros [59-62] and buffer layers for HTc superconductors; in particular, high quality [001] cubic YSZ (Yttria-Stabilised Zirconia) may be grown on Silicon substrates to promote the epitaxial growth of c⊥ YBCO, since a and b YBCO axes match YSZ along the cube face diagonal ([110] and [$1\bar{1}0$]) [1,63]. Other interesting applications have been proposed, which take advantage from the thermo-mechanical properties of zirconia to realise protective layers on metal components exposed to harsh environment and high temperature corrosion [64-68,14]. In general, depending on the applications, zirconia thin films may be realised by different processes and with different microstructure; a high texture probably is not a required quality for protective coatings, but may be of paramount

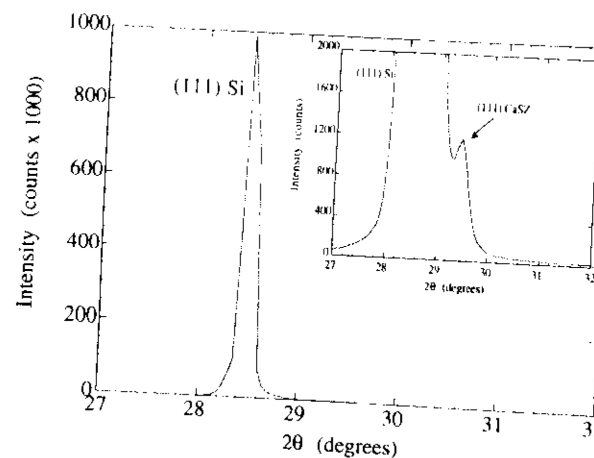

Figure 29. XRD pattern of CaSZ on <111> Si.

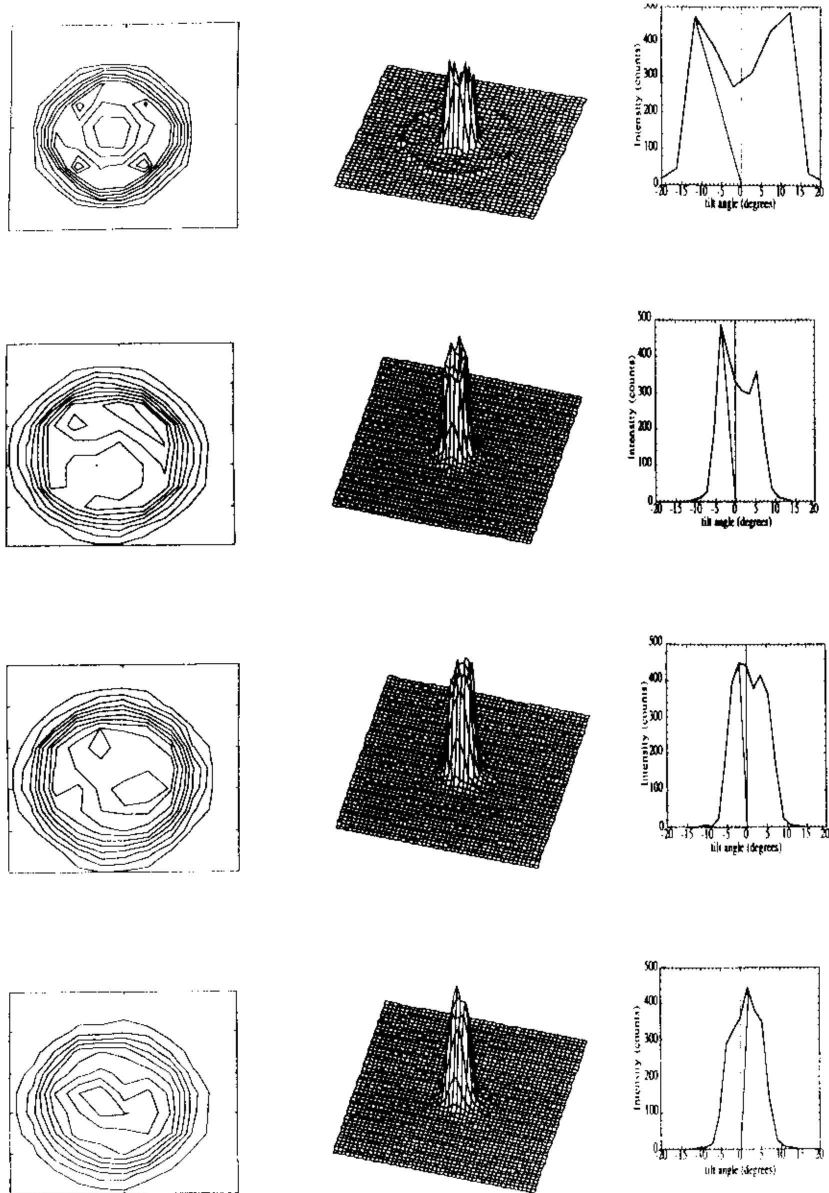

Figure 30. (111) CaSZ pole figures taken on different spots of a 7.5 cm Si wafer; from left to right: 2D, 3D and linear cross section. From top to bottom: h=0 (centre), h=7, h=15 and h=20 mm

importance for YBCO buffer layers.

Considering PVD techniques, thin film microstructure of oxides is much influenced by the deposition temperature; in general, highly oriented films are produced at high substrate temperatures, whereas texture is more complex after room temperature (RT) deposition, which can even produce amorphous layers. In the following, it will be presented the result of the characterisation of CaO-stabilized zirconia (CaSZ) thin films deposited at RT on <111> Si by r.f. magnetron sputtering [38,69]; despite the completely different features with respect to the epitaxial $SrTiO_3$ and YBCO films, the XRD methods described in previous paragraphs can be used with success to give a detailed picture of the microstructure.

Independently of the working gas (Ar) pressure, the BB pattern of CaSZ thin films deposited at RT show only the (111) CaSZ reflection strongly overlapped with the intense (111) substrate peak (Figure 29), and the weak second order (222) CaSZ peak; apparently, BB patterns would suggest a [111] CaSZ ‖ [111] Si orientation, but a different picture comes out in the (111) CaSZ pole figure. Figure 30 shows the pole figures taken at different positions on a 7.5 cm wafer coated with 720 nm of CaSZ by using an r.f. magnetron sputtering equipped with a 7.5 cm CaSZ target [38] (Figure 31). For each position, 2D (left) and 3D (centre) plots are displayed along with a linear cross section through the centre (right). In the middle of the wafer (h=0 mm) the 2D pole figure is axially symmetric, with a toroidal shape, and a maximum at ~13° from the surface normal ([111] Si). Moving along the wafer radius (h=7 mm) the pole figure becomes asymmetrical, with the maximum inclined ~4°; then, between h=15 mm and h=20 mm, the figure is roughly symmetrical and has a maximum about 0°. This type of texture suggests that the growth mechanism is not associated to an epitaxial relationship between <111> Si and CaSZ; the same kind of texture was observed on <100> Si substrates [69], therefore it seems correct the hypothesis that growth is not epitaxial, but simply proceeds with the closest packing

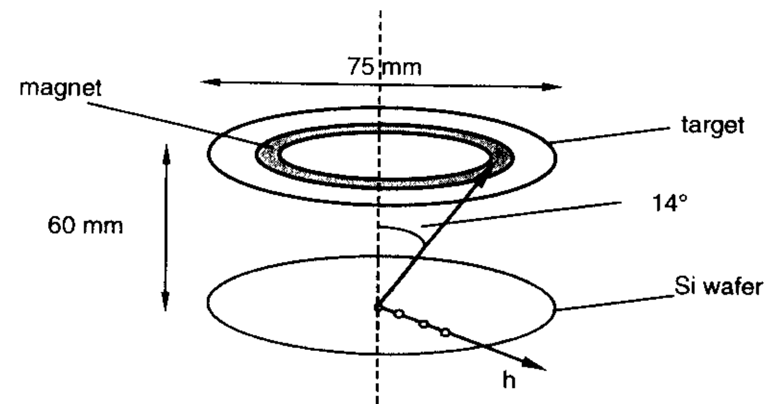

Figure 31. Schematic of the r.f. magnetron sputtering system [69].

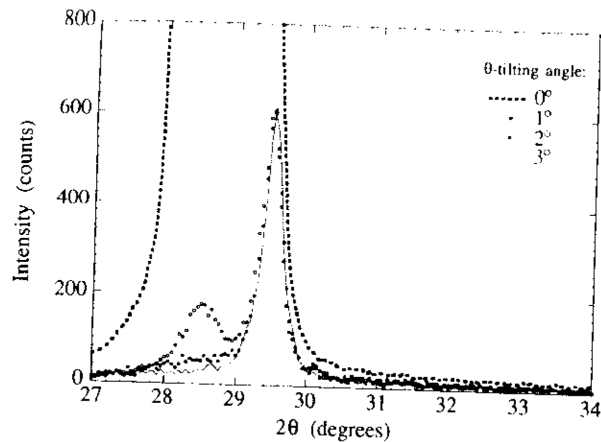

Figure 32. XRD patterns of the CaSZ sample of Figure 29, taken at different θ-tilting angles.

(111) CaSZ planes perpendicular to the direction of the maximum flux impinging the substrate. The low (RT) temperature does not permit any reorganisation of atoms on the surface, hence the growth is preferentially along the direction connecting substrate and maximum sputtering region, i.e., the region of the annular magnet (Figure 31); considering a 7.5 cm target, 6 cm target to substrate distance and 3 cm magnet diameter, the maximum flux impinging substrate centre is inclined to atn(1.5/6)≈14°, in good agreement with the pole figure maximum of ~13°.

In this case both crystallite size and defect density should be deeply influenced by the lack of an epitaxial growth, which led to an axially symmetrical (fibre) texture. As shown in Figure 29, the strong overlapping between (111) CaSZ and (111) Si does not permit to carry out a reliable LBA; however, it is possible to reduce down to zero the substrate signal, exploiting the very high texture of the single crystal substrate, with respect to the film. In fact, by tilting the sample of a few degrees (θ-tilting), the (111) Si diffracted signal decreases abruptly, while the (111) CaSZ peak is not sensibly affected; as shown in Figure 32, a 3° θ-tilting is enough to cancel the substrate signal. The little defocusing error introduced in this way is not such to change significantly the instrumental profile, so that a reliable LBA may be conducted on (111) and (222) CaSZ [69].

The crystallite size distributions were broad, with an average value of 13-23 nm for thin films deposited at 1.5 kV in the range 1×10^{-2} - 1×10^{-3} mbar of working gas pressure, respectively. As shown in Figure 33, besides being broad, the size distribution clearly shows two maxima to ~5 nm and ~25 nm. The microstrain is a strongly varying function of L, and the average value at $L=\overline{M}/2$ ranges between 0.0045 and 0.0034 in the range 1×10^{-2} - 1×10^{-3} mbar, respectively. Therefore, from LBA we may conclude that in this case the microstructure is not as ordered as that of epitaxial thin films, and a high defect density and a broad distribution of grain size and shape should be present.

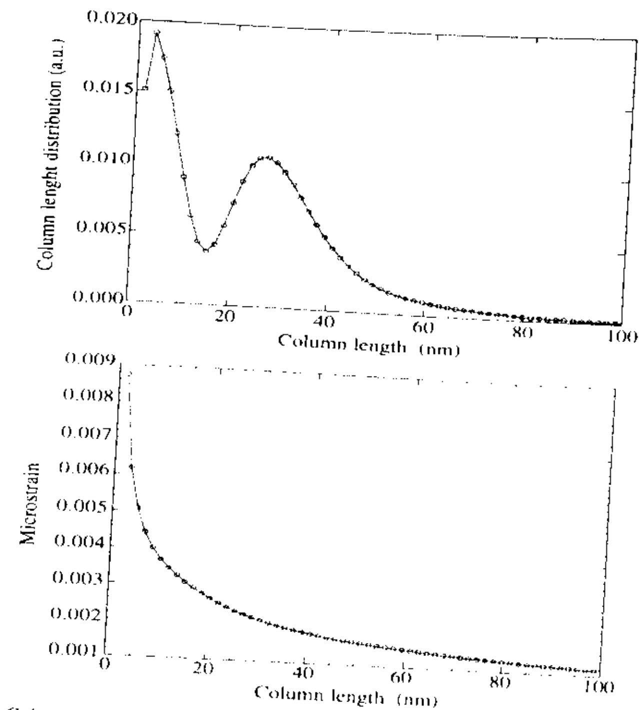

Figure 33. Column length and microstrain distribution from LBA of the CaSZ sample of Figure 32.

All these results were confirmed by TEM analysis. As shown in Figure 34, both bright and dark field images display a complex microstructure, with small grains at the interface with the substrate, where a thin (~4 nm) amorphous SiO_2 layer is present. Starting from this nanocrystalline CaSZ layer, large columnar grains grow toward the surface, with size ranging from a few nm to ~100 nm. The polycrystalline nature of the film was confirmed also by the SAD (Selected Area Diffraction), which also shows a further detail; as schematically depicted aside, the 111 spot is broadened over an angular region between -20 and +15°, with a maximum at ~13°. Therefore, the columnar grains tend to be oriented along a direction ~13° from the surface normal, while the nanocrystals are roughly random oriented; this picture is in a perfect agreement with the predictions of both LBA (Figure 33) and texture analysis (Figure 30).

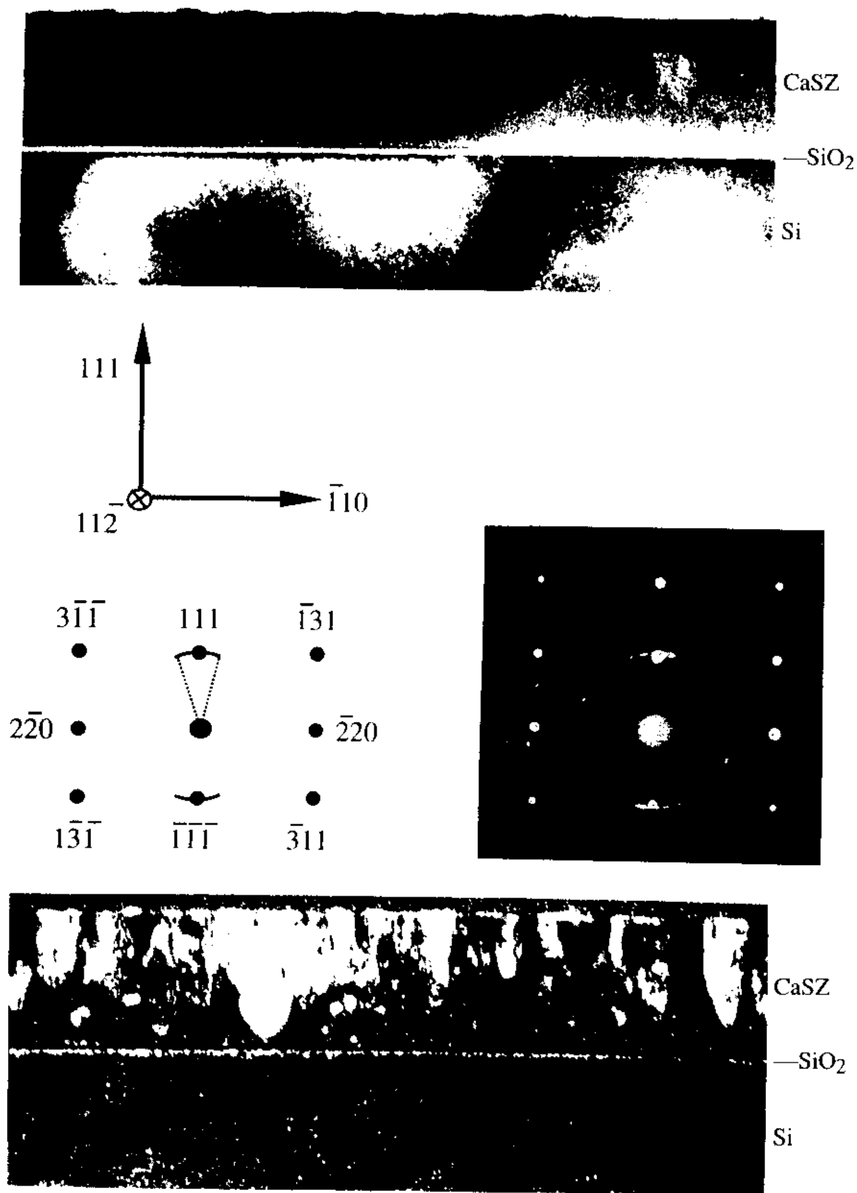

Figure 34. TEM of a cross section CaSZ thin film. Bright field (top) dark field (down) and SAD (middle)

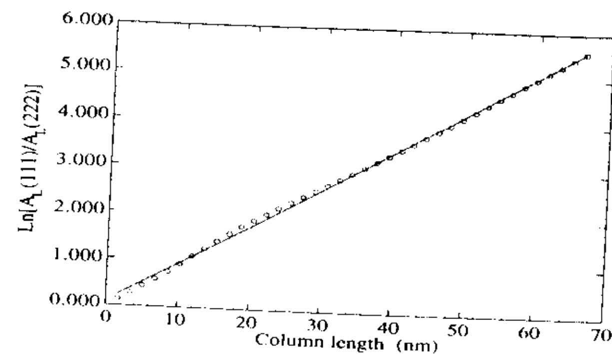

Figure 35. VHH plot for the sample of Figure 33.

In order to make some hypothesis on the dominant type of defect present in the film, we may apply the VHH method (see §3). As shown in Figure 35 for the film of Figures 33 and 34, the trend of $\ln[A_L(h)/A_L(h+1)]$ versus L was always linear, suggesting the presence of a microstrain field $<\varepsilon^2(L)>\propto 1/L$, which can be attributed to the presence of dislocations. Even though it must be underlined again that the predictions of this analysis are not univocal, it makes sense that the main defects present in these films are dislocations, resulting from growth and adaptation of grains with different size, shape and orientation within a disordered microstructure.

5. Conclusions

XRD techniques are a useful tool to study the microstructure of thin films. This paper was aimed to demonstrate the effectiveness of some XRD methods to this purpose, using traditional XRD equipment like Bragg-Brentano and 4-circle goniometers. Two types of analysis have been discussed, which are both of interest to thin film microstructural characterisation: line broadening analysis (LBA) and texture analysis. The former can be conducted by using traditional non-dedicated BB diffractometers, and gives information on lattice disorder, whereas the latter concerns growth mechanisms and epitaxial relationships between thin film and substrate.

It was shown that typical epitaxial thin films like $SrTiO_3$ buffers and YBCO HT_c thin films have a columnar grain structure, whose height distribution can be investigated by LBA; lattice defects may also be studied by LBA, which can support hypotheses on their nature and distribution within thin film microstructure. Pole figures were measured on buffers and superconducting thin films to study their texture; to this purpose, it was shown that BB patterns and Ω-scan are also useful tools, even though they do not guarantee an exhaustive information on grain orientation. Both lattice disorder and texture have been

shown to have a deep influence on important superconducting properties like T_c and J_c; moreover, a careful characterisation of the buffer layer is extremely important to understand and improve superconducting top layer quality.

This kind of approach to thin film study, can be applied to any other epitaxial thin films system. In addition, these XRD techniques may also be useful to study polycrystalline non-epitaxial thin films; to show this, the complex microstructure of stabilised zirconia thin film deposited at room temperature on Si wafers by r.f. magnetron sputtering was described in detail by LBA and pole figure analysis. This latter example, validated by a TEM analysis, showed the possibility of studying also thin films with complex grain size, shape and texture.

Acknowledgements

The author wishes to thank G. Cappuccio, L. Correra, F.C. Matacotta and P.G. Orsini for useful discussions, and S. Setti and M. Baldessari for technical help during XRD measurements; the author is in debt to A. Migliori and C. Della Volpe who kindly supplied with TEM and AFM pictures, respectively.

References

1. D.K. Fork, S.M. Garrison, M. Hawley, T.H. Geballe, *J. Mat. Res.* **7** (1992) 1641.
2. S.S. Laderman, R.C. Taber, R.D. Jacowitz, J.L. Moll, C.B. Eom, T.L. Hylton, A.F. Marshall, T.H. Geballe and M.R. Beasley, *Phys. Rev.* **B43** (1991) 2922.
3. A. Lamagna, S. Nicoletti, M. Sanchez Balmaseda, A. Migliori, R. Fabbri and L. Correra, *Supercond. Sci. Technol.* **5** (1992) 117.
4. D.C. Kothari, P. Scardi, S. Gialanella and S. Guzman, *Philos. Mag.*, **61** (1990) 627.
5. P. Scardi, D.C. Kothari, L. Guzman, *Thin Solid Films,* **195** (1991) 213.
6. P. Scardi, L. Lutterotti, L. Correra and S. Nicoletti, *J. Mat. Res.*, **8** (1993) 2780.
7. R. Felder and B.S. Berry, *J. Appl. Cryst.* **3** (1972) 372.
8. A.J. Perry, V.V. Valvoda and D. Rafaja, *Thin Solid Films* **214** (1992) 169.
9. M.F. Toney, T.C. Huang, S. Brennan, *J. Mat. Res.* **3** (1988) 351.
10. A. Segmuller, I.C. Noyan and S. Speriosu, *Prog. Crystal Growth and Charact.* **18** (1989) 21.
11. C.J. Shute and J.B. Cohen, *J. Appl. Phys.* **70** (1991) 2104.
12. G. Cappuccio, M. Leoni, P. Scardi, V. Sessa, L. Terranova, *Mater. Sci. Forum* (1995). Submitted.
13. L. Lutterotti, P. Scardi and A. Tomasi, *Mater. Sci. Forum* **133-136** (1993) 57.
14. P. Scardi, L. Lutterotti and A. Tomasi, *Thin Solid Films* **236** (1993) 130.
15. P. Scardi, L. Lutterotti and P. Maistrelli, *Powder Diffraction* **9** (1994) 180.
16. P. Scardi. (1994). Unpublished results.
17. H.R. Wenk, *J. Appl. Cryst.*, **25** (1992) 524.
18. S.M. Garrison, N. Newman, B.F. Cole, K. Char and R.W. Barton, *Appl. Phys. Lett.* **58** (1991) 13.
19 J.Y. Wang, L.G. Wang, C.C. Young and S.E. Hsu, *Mat. Chem. and Phys.* **32** (1992) 295.

20. B.E. Warren and B.L. Averbach *J. Appl. Phys.* **21** (1950) 595.
21. B.E. Warren and B.L. Averbach *J. Appl. Phys.* **23**(1952) 1059.
22. G.K. Williamson and W.H. Hall, *Acta Met.* **1** (1953) 22.
23. G.K. Williamson and R.E. Smallman, *Phil. Mag.* **1** (1956) 34.
24. B.E. Warren, *X-ray Diffraction* (Addison-Wesley, Reading, MA, 1969), pp.251-314.
25. H.P. Klug and L.E. Alexander, *X-ray Diffraction Procedures for Polycrystalline and Amorphous Materials* (Wiley, New York, 1974), 2nd ed., pp 642-708
26. S. Enzo, G. Fagherazzi A. Benedetti and S. Polizzi, *J. Appl. Cryst.* **21** (1988) 536.
27. A. Benedetti, G. Fagherazzi S. Enzo and M. Battagliarin, *J. Appl. Cryst.* **21** (1988) 543.
28. P. Scardi, L. Lutterotti, R. Di Maggio, *Powder Diffraction* **6** (1991) 20.
29. P. Scardi *et al.*. Unpublished results.
30. A.R. Stokes, *Proc. Phys. Soc.* **A61**(1948) 382.
31. D. Balzar, *J. Appl. Cryst.* **25** (1992) 559.
32. R.J. Matyi, L.H. Schwartz and J.B. Butt, *Catal. Rev. -Sci. Eng.* **29** (1987) 41.
33. W.L. Smith, *J. Appl. Cryst.* **5** (1972) 127.
34. W.L. Smith, *J. Appl. Cryst.* **9** (1976) 139.
35. C.J. Shute and J.B. Cohen, *J. Mat. Res.*, **6** (1991) 950.
36. A.J. Perry, M. Jagner, W.D. Sproul and P.J. Rudnik, *Surf. Coat. Technol.*, **39-40** (1989) 387.
37. A.J. Perry, M. Jagner, P.F. Woerner, W.D. Sproul and P.J. Rudnik, *Surf. Coat. Technol.*, **43-44** (1990) 234.
38. P. Scardi, P. Polonioli and S. Ferrari, *Thin Solid Films*, **253** (1994) 349.
39. I.C. Noyan and J.B. Cohen, *Residual Stress, Measurement by Diffraction and Interpretation* (Springer, New York, 1987).
40. J.I. Langford, A. Boultif, J.P. Auffredic and D. Louer, *J. Appl. Cryst.* **26** (1993) 22.
41. S.I. Rao and C.R. Houska, *Acta Cryst.* **A42** (1986) 6
42. S.I. Rao and C.R. Houska, *Acta Cryst.* **A42** (1986) 14
43. M.A. Krivoglaz, O.V. Martynenko and K.P. Ryaboshapka, *Phys. Met. Metall.* **55** (1983) 1.
44. R. Kuzel Jr and P. Klimanek, *J. Appl. Cryst.* **22** (1989) 299.
45. R.K. Nandi, H.K. Kuo, W. Schlosberg, G. Wissler, J.B. Cohen and B. Crist Jr, *J. Appl. Cryst.* **17** (1984) 22.
46. R.L. Rothman and J.B. Cohen, *Adv. X-ray Anal.* **12** (1969) 208
47. W. Vogel, J. Haase and R. Hosemann, *Z. Naturforsch.*, **A29** (1974) 1152.
48. J.G. Bednorz and K.A. Müller, *Z. Phys. B.: Condens. Matter* **64** (1986) 189.
49. N.G. Dhere, in *Thin Films for Emerging Applications*, ed. M.H. Francombe, J.L. Vossen. Vol 16 of *Physics of Thin Films* (Academic Press, S.Diego, 1992).
50. M.V. Sidorov, S.R. Oktyabrsky and S.I. Krasnosvobodtsev, *Mat. Sci. & Eng.* **B18** (1993) 295.
51. Powder Diffraction File, Swarthmore, PA, International Centre for Diffraction Data (1988); card # 35-734

52. J. Ye and K. Nakamura, *Phys. Rev.* **B50** (1994) 1
53. Powder Diffraction File, Swarthmore, PA, International Centre for Diffraction Data (1988); card # 38-1433. See also:*Powder Diffr.* **2** (1987).
54. D. Balzar, H. Ledbetter, *J. Mat. Sci. Lett.* **11** (1992) 1419.
55. M. Bianconi, G. Bobbio, L. Correra, A. Lamagna, S. Nicoletti, M. Sanchez Balmaseda and W. Soncini, *Mat. Sci. & Eng.* **B13** (1992) 21.
56. L. Correra, S. Nicoletti, S. Neri, F. Arcidiacono, P. Scardi, in *Report on Buffer and Passivation Layers Deposition*, ESPRIT Project 6625 - X BAND PRO (CEC, 1994).
57. V.I. Dediu, Q.D. Jiang, F.C. Matacotta, P. Scardi, M. Lazzarino, G. Nieva, L. Civale, *Superc. Sci. and Techn.* (1995). In press.
58. P. Scardi, F.C. Matacotta, L. Correra. (1995). Unpublished results.
59. W.H.Lowdermilk, D.Milam and F.Rainer, *Thin Solid Films* **73** (1980) 155;
60. W.T.Pawlewicz, D.D.Hays and M.Martin, *Thin Solid Films* **73** (1980) 169;
61. K.V.S.R.Apparao, N.K.Sahoo and T.C.Bagchi, *Thin Solid Films* **129** (1985) L71;
62. Y.Miyahara, K.Tsukada and H.Miyagi, *J. Appl. Phys* **63** (1988) 2431.
63. W.Shi, J.Shi, W.Yao, Zh.Qi, Sh.Tang, G.Zhou, *Thin Solid Films* **203** (1991) 267.
64. R. Di Maggio, P. Scardi and A. Tomasi *Mat. Res. Soc. Symp. Proc.* **180** (1990) 481.
65. A.Tomasi, P.Scardi and F.Marchetti, *Mat. Res. Soc. Symp. Proc.* **271** (1992) 477.
66. R. Di Maggio, A. Tomasi, P. Scardi and F. Marchetti, in *Euro-Ceramics II, Structural Ceramics and Composites*, ed. by G. Ziegler and H. Hausner, (Deutsche Keramische Gesellschaft e.V., Kohln, 1991). Vol. 2, p. 1745.
67. R. Di Maggio, P. Scardi and A. Tomasi, *Mat. Engineering*, **5** (1994) 13.
68. A.S.Kao and C.Hwang, *J. Vac. Sci. Technol.* **A8** (1990) 3289.
69. S. Ferrari and P. Scardi, in *Advances in Inorganic Films and Coatings*, ed. P. Vincenzini (Techna, Faenza, 1995). In press.